J. Fluid Mech. (1985), *vol.* 154, *pp.* 163–185
Printed in Great Britain

Simulation of blunt-fin-induced shock-wave and turbulent boundary-layer interaction

By CHING-MAO HUNG AND PIETER G. BUNING
Computational Fluid Dynamics Branch, NASA Ames Research Center,
Moffett Field, California

(Received 27 February 1984)

The Reynolds-averaged Navier–Stokes equations are solved numerically for supersonic flow over a blunt fin mounted on a flat plate. The fin shock causes the boundary layer to separate, which results in a complicated, three-dimensional shock-wave and boundary-layer interaction. The computed results are in good agreement with the mean static pressure measured on the fin and the flat plate. The main features, such as peak pressure on the fin leading edge and a double peak on the plate, are predicted well. The role of the horseshoe vortex is discussed. This vortex leads to the development of high-speed flow and, hence, low-pressure regions on the fin and the plate. Different thicknesses of the incoming boundary layer have been studied. Varying the thicknesses by an order of magnitude shows that the size of the horseshoe vortex and, therefore, the spatial extent of the interaction are dominated by inviscid flow and only weakly dependent on the Reynolds number. Coloured graphics are used to show details of the interaction flow field.

1. Introduction

In high-speed space vehicle design, the impingement of a shock wave on a downstream surface is one of the most severe aerodynamic problems encountered. It may result in loss of control effectiveness owing to flow separation or in loss of structural integrity owing to severe local heating. Many different types of shock-impingement interactions have been observed. In some instances, such as the bow shock from the shuttle nose impinging on the wing leading edge, the inviscid effects are dominant, and the strength and location of the impinging shock are known. More frequently, however, viscosity is of prime importance, and the shock impingements result from an inviscid–viscous flow interaction. To add complexity to the problem, neither the shock strength nor the location of the impingement are known beforehand.

A frequently encountered problem of this type occurs when a high-speed flow passes over a blunt fin mounted on a surface (figure 1). The fin bow shock causes the boundary layer to separate from the surface ahead of the fin, resulting in a separated-flow region composed of horseshoe vortices near the surface, and a lambda-type shock pattern ahead of the fin. The shock wave emanating from the separated-flow region (separation shock) impinges on the fin bow shock, and causes intense heating and high pressure locally around the fin leading edge (discussed later).

Owing to the complexity of the flow phenomena, almost all previous studies have been experimental (e.g. Price & Stalling 1967; Kaufman, Korkegi & Morton 1972; Sedney & Kitchens 1975; Dolling & Bogdonoff 1982; and Ozcan 1982). In general, because of considerations of time and economy, measurements are only carried out

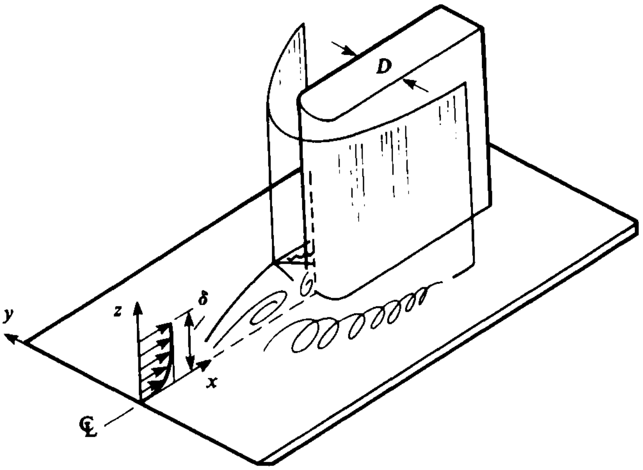

FIGURE 1. Blunt fin on a flat plate.

on the body surface and in the plane of symmetry. With the advent of large and fast vectorized computers, solving numerically a general three-dimensional flow field is now feasible. The objectives of computational fluid dynamics are now not only to calculate the flow field, but also to gain an understanding of the physics of the flow. The purposes of the present article are to employ a numerical technique previously developed by Hung & Kordulla (1984) to simulate a high-speed flow passing over a blunt fin mounted on a flat plate and, with all the data in hand, to study the detailed features of the interaction of the blunt-fin-induced shock wave and turbulent boundary layer.

Experiments conducted by Dolling, Cosad & Bogdonoff (1979) and Dolling & Bogdonoff (1982) at a free-stream Mach number of 2.95 and a unit Reynolds number of 6.3×10^7 m^{-1} will be used for comparison. Two lengthscales are associated with this interaction flow field: one is the diameter of the blunt fin D and the other is the incoming boundary-layer thickness δ. In the present study, the thickness of the boundary layer will be varied from $\delta/D = 1.0$ to 0.1 to demonstrate the weak dependence on Reynolds number of the spatial extent of the interaction, as observed in the experiments. Computed results will first be compared with measurements of surface pressure on the flat plate and on the fin. Some of the results for the $\delta/D = 1.0$ case have previously been presented in the article by Hung & Kordulla (1984) to verify the program development. The physical aspects of the flow field will be stressed in the present study. The existence and the role of a horseshoe vortex and two reversed supersonic zones is also discussed. Coloured graphics of the pressure and Mach number in various planes will show the detailed structure of the mean flow field.

Some caution is required here. Most experiments have observed certain degrees of unsteadiness in this type of flow field, as well as other types of shock wave and turbulent boundary-layer interactions. Dolling & Bogdonoff (1981) investigated the unsteady behaviour of the flow field for the case of $\delta/D = 0.26$ and pointed out that the flow is inherently unsteady. However, as shown by that and other unsteady-flow studies (for instance Hayakawa, Smits & Bogdonoff 1984), this unsteadiness is an irregular, broad-band and completely stochastic fluctuation which is associated with the dynamic nature of the turbulent boundary layer. Sedney & Kitchens (1975) pointed out that the dominant frequency of the oscillation is probably of the order of 1000 Hz. This oscillation can only be resolved by a direct or large-eddy turbulence simulation. Thus, for the present study, the Reynolds-averaged Navier–Stokes equations are used and the random turbulence fluctuations are suppressed. The comparison of computational results with the experimental measurements is made only in terms of 'mean' values, which is within the scope of the Reynolds-averaged approach. Further experimental studies of shock wave and turbulent boundary-layer interaction will help future developments of turbulence modelling, but the age of direct, time-dependent turbulence simulation of this type of problem is still some way away.

2. Numerical procedure

2.1. *Equations in non-dimensional form*

In the absence of body forces and source terms, the governing Navier–Stokes equations for conservation of mass, momentum and energy in a stationary, finite volume $\mathcal{V}$, enclosed by the control surface $\mathcal{S}$, can be written in non-dimensional form as

$$\frac{\partial}{\partial t}\int_{\mathcal{V}} \boldsymbol{q}\,\mathrm{d}\mathcal{V} + \int_{\mathcal{S}} (\boldsymbol{q}\boldsymbol{u}+\mathcal{B})\cdot\boldsymbol{n}\,\mathrm{d}\mathcal{S} = 0,$$

where

$$\begin{aligned}
\boldsymbol{q} &= (\rho, \rho u, \rho v, \rho w, \rho E)^{\mathrm{T}},\\
E &= e_{\mathrm{i}}+\tfrac{1}{2}(u^2+v^2+w^2),\\
\mathcal{B} &= (\boldsymbol{b}_\rho, \boldsymbol{b}_m, \boldsymbol{b}_e)^{\mathrm{T}},\\
\boldsymbol{b}_\rho &= 0,\\
\boldsymbol{b}_m &= p\boldsymbol{I}+M_\infty Re_D^{-1}\boldsymbol{\tau},\\
\boldsymbol{\tau} &= -\lambda\,\mathrm{div}\,\boldsymbol{u}\boldsymbol{I}-\mu[(\mathrm{grad}\,\boldsymbol{u})+(\mathrm{grad}\,\boldsymbol{u})^{\mathrm{T}}],\\
\boldsymbol{b}_e &= -\gamma M_\infty (Re_D\,Pr)^{-1}\mu\,\mathrm{grad}\,e_{\mathrm{i}}+p\boldsymbol{u}+M_\infty Re_D^{-1}\boldsymbol{\tau}\cdot\boldsymbol{u}.
\end{aligned}$$

Here conventional definitions of the flow quantities are used. The Cartesian velocity components (u, v, w) are normalized by the free-stream speed of sound a_∞, ρ is normalized by ρ_∞, the specific internal energy e_{i} and total energy E are normalized by a_∞^2, and p is normalized by $\rho_\infty a_\infty^2$. The two viscosity coefficients λ and μ are normalized by the molecular viscosity μ_∞. The constant γ is the ratio of specific heats, Re_D is the Reynolds number based on free-stream velocity and diameter D, and Pr is the Prandtl number. For a perfect gas the normalized state relations are

$$p = \frac{1}{\gamma}\rho T, \quad e_{\mathrm{i}} = \frac{T}{\gamma(\gamma-1)}, \quad a^2 = T,$$

where the temperature T is normalized with respect to T_∞. The above system of equations is valid for turbulent as well as laminar flow by replacing the molecular-transport coefficients with their turbulent counterparts. (It becomes the so-called Reynolds mass-averaged Navier–Stokes equations.) Sutherland's formula is used to evaluate the molecular viscosity. A turbulence model closes the system of governing equations.

For high-Reynolds-number flows, the viscous effects are confined to a thin layer near the wall boundary and are dominated by the viscous terms associated with the strain rates normal to the wall. The viscous terms associated with the strain rates along the body are comparatively small and negligible. This concept was first discussed by Prandtl in the development of boundary-layer theory and has been applied and extended to various problems. The development of the thin-layer approximation by Baldwin & Lomax (1978) is based on this concept, with the retention of the unsteady and all the inviscid terms of the Navier–Stokes equations. The extension of the thin-layer approximation to two directions was demonstrated in a previous study of supersonic flow over an axial corner (Hung & Kuraski 1980). Here, the concept is extended to the case of thin layers in all three directions for a general coordinate system. All the viscous terms associated with cross-derivatives are neglected, but with retention of terms with normal second derivatives. This approximation retains not only the most dominant terms in the governing equation but also the so-called 'second-order' boundary-layer terms as derived by Rubin (1966). The neglected cross-derivatives can be of the same order of magnitude as the retained normal derivatives very near the junction of two walls, but the flow contains comparatively very low momentum. Therefore, neglect of cross-derivatives will not significantly affect the general features of the flow field.

A numerical procedure previously developed by Hung & Kordulla (1984) is adopted. The program is coded for general three-dimensional body-fitted coordinates. A cell-concept finite-volume formulation is implemented. The computational domain is divided into a number of non-overlapping finite cells prescribed by surrounding grid points. The cell surface and volume are accurately evaluated, and the resulting solution satisfies the integral conservation laws of mass, momentum and energy. The basic numerical scheme is MacCormack's (1982) explicit–implicit predictor–corrector algorithm with a Strang-type (1968) time-splitting. The time-splitting makes the method locally one-dimensional for three-dimensional problems and also makes the dependent variables on the right-hand side consistent with the characteristic variables in a similarity transformation. The thin-layer approximation drastically simplifies the evaluation of viscous diffusion and dissipation terms, and allows easy vectorization of the algorithm. Details of the numerical technique are discussed by Hung & Kordulla (1984).

2.2. *Mesh system*

For a simple geometry, such as a fin on a flat plate, the mesh can be algebraically generated for easy control of mesh spacing and distribution. For the present study at zero angle of attack the flow is assumed to be symmetrical with respect to the centreplane of the fin; hence only half of the flow is calculated. Figure 2 shows a mesh system of $40 \times 32 \times 32$ points, in which the I-direction corresponds to the coordinate along the fin, the J-direction is outward from the fin, and the K-direction is normal to the flat plate. The origin is set at the nose-tip of the fin on the flat plate. In both the J- and K-directions (the outward and the z-direction), the mesh is geometrically stretched. A fine mesh near the wall is required for an adequate resolution of the viscous effects.

In an (x, y)-plane, the mesh is basically oriented along polar coordinates in the nose region and along Cartesian coordinates in the straight fin region. Along the fin body in the I-direction, equal spacing is used in the nose region and geometrically stretched spacing from the shoulder to the downstream boundary. At the outer boundary a geometric stretching formula is used to blend the mesh system from a polar coordinate mesh to a normal Cartesian mesh. The blending procedure avoids abrupt changes in cell size, but results in a slightly non-orthogonal mesh in that region, as shown in figure 2.

2.3. *Boundary conditions*

The fin is assumed semi-infinite in height and length, so that zero-gradient boundary conditions are imposed at the outer boundaries in the corresponding directions. The

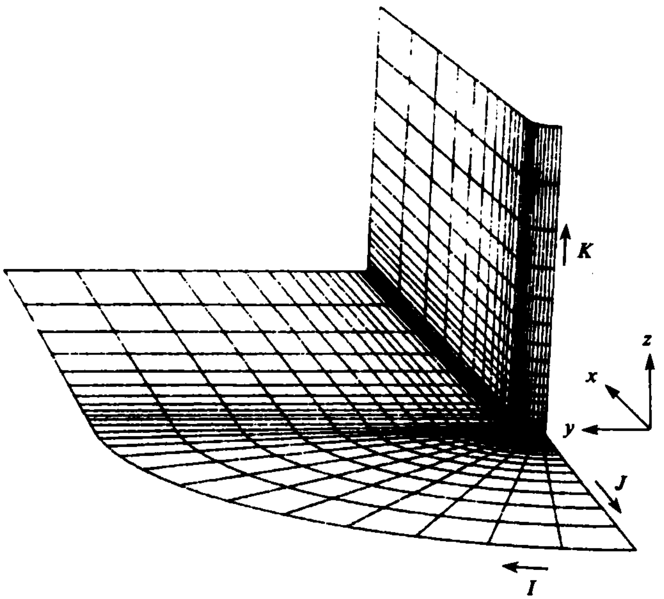

FIGURE 2. Mesh distribution on blunt fin and flat plate.

fin is at zero yaw, and a symmetry condition is imposed at the plane of symmetry. The wall is assumed impermeable, and no-slip boundary conditions are applied. The wall is also assumed to be adiabatic, and the pressure gradient normal to the wall is set to zero.

The outer boundary of $J = J_{\max}$ is set far enough away to avoid any influence on the interaction region. Theoretically one can prescribe a boundary-layer profile on the flat plate at each x-location along the outer boundary. These profiles can be easily generated from their corresponding points of a flow over an isolated flat plate as sketched in figure 3. In the present calculation, the range of interest is assumed small compared to the length of flat plate generating the incoming boundary. Hence, the variation of the boundary-layer profile at the outer boundary is assumed small and is neglected. Therefore one predetermined boundary-layer profile is prescribed for all x-locations along the outer boundary.

2.4. *Turbulence model*

Turbulence modelling for the three-dimensional configuration of figure 1 is complicated and not well developed. As $z \rightarrow \infty$, turbulence is dominated by the fin surface; on the other hand, as $z \rightarrow 0$, the turbulence is under the influence of the flat plate. Near the junction, the turbulence is completely three-dimensional.

Turbulent transport described here used the eddy-viscosity concept, and empirical models are used to determine the transport coefficients. To simplify the analysis in the present study, an algebraic eddy-viscosity model, proposed by Baldwin & Lomax (1978), with a 'modified distance' is used. This model is particularly well suited for complex flows that contain regions in which the lengthscales are not clearly defined. No attempt is made at present to account for the history and the amplification of turbulence intensity after a sudden strong compression through a shock wave. The study of more realistic or complex turbulence models is left for future study.

In each (J, K)-plane, the computational domain is similar to a corner formed by

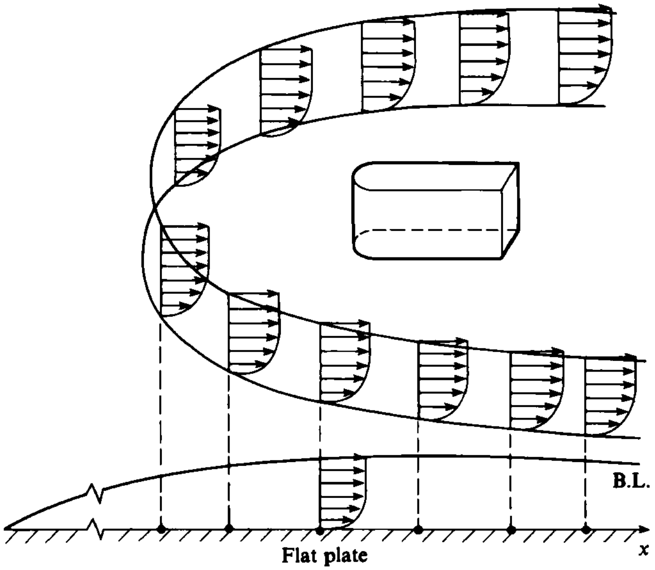

FIGURE 3. Boundary-layer profiles on the flat plate at x-locations.

two perpendicular walls, as sketched in figure 4. For simplicity of discussion (y, z) are used as coordinates. The two-layer turbulence model developed by Baldwin & Lomax (1978) is applied in the following way: In the inner region, the Prandtl mixing-length expression is

$$\epsilon_{\text{inner}} = \rho(\kappa \mathscr{D} \eta)^2 \omega,$$

where $\mathscr{D}$ is the van Driest damping factor, κ is von Kármán's constant, and ω is the absolute value of vorticity $\omega = |\nabla \times V|$. This formula is similar to the model of Cebeci & Smith (1974), except for the use of the absolute value of vorticity, which is invariant with respect to the coordinate system and thus avoids complication in the corner region. The definition of distance η is critical for evaluation of the lengthscale in the eddy-viscosity model. For the present analysis, a modified distance developed in an earlier investigation of a three-dimensional corner (Hung & MacCormack 1979) is adopted:

$$\eta = \frac{2yz}{y+z+(y^2+z^2)^{\frac{1}{2}}}.$$

This formula is designed to account for the size of turbulence eddies or the turbulence mixing length near the corner under the influence of both walls. Note that, as $z/y \rightarrow \infty$, $\eta \rightarrow y$, and, as $y/z \rightarrow \infty$, $\eta \rightarrow z$.

In the outer region,

$$\epsilon_{\text{outer}} = C_{\text{cp}}(0.0168 \rho F_{\text{wake}} \beta),$$

where

$$F_{\text{wake}} = \text{the smaller of} \begin{cases} \eta_{\max} F_{\max}, \\ C_{\text{wk}}\, \eta_{\max}\, u_e^2 / F_{\max}. \end{cases}$$

The quantity $F_{\max}$ is the maximum value of $F(\eta) = \eta \omega \mathscr{D}$, and $\eta_{\max}$ is the value of η at which it occurs. The Klebanoff intermittency factor β is given by

$$\beta = \left[1 + 5.5\left(\frac{C_{\text{Kleb}}\, \eta}{\eta_{\max}}\right)^6\right]^{-1}.$$

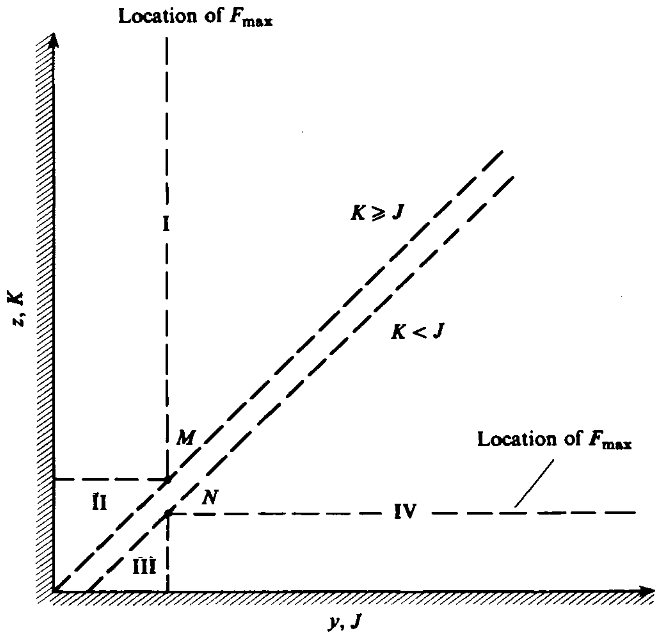

FIGURE 4. Division of four regions in (J, K)-plane.

The constants appearing in the preceding relations are

$$C_{cp} = 1.6, \quad C_{wk} = 0.25, \quad C_{Kleb} = 0.3.$$

The plane is divided into four regions I, II, III, and IV as shown in figure 4. In regions I and II, $\mathscr{D}$ is evaluated at wall $y = 0$ and, in III and IV, $\mathscr{D}$ is evaluated at the wall $z = 0$. The search for F_{max} and its corresponding η_{max} proceeds outward from the wall, either from $y = 0$ for region IV, or from $z = 0$ for region I. The values of F_{max} in regions II and III are constants, equal to the value of F_{max} at M and N, respectively.

3. Results and discussion

The flow to be simulated has free-stream conditions of $M_\infty = 2.95$, and unit Reynolds number of 6.3×10^7 m^{-1}. A blunt fin of diameter $D = 1.27$ cm is at zero yaw, as shown in figure 1. There are two lengthscales involved in the flow field. One is the diameter of the blunt fin and the other is the incoming boundary-layer thickness. The diameter is a geometric parameter that determines, for instance, the inviscid bow-shock shape and location. The incoming boundary-layer thickness is a viscous flow-field parameter and depends on the Reynolds number. Very often in the interaction of a two-dimensional shock wave and boundary layer (see e.g. Horstman *et al.* 1977), the boundary-layer thickness is one of the most important parameters affecting the size of the separation bubble and the range of upstream influence. In a three-dimensional flow, there is an additional direction for the fluid to move and escape from a severe adverse environment. Consequently, not only the boundary-layer thickness, but other factors arising from the extra dimension will affect the extent of the interaction. The question is, what is the role each one plays, and which one is the dominant parameter?

In the present paper, the surface properties and features of the flow field in the plane of symmetry will be shown first and compared with experimental measurements for the case of $\delta/D = 1.0$. Then the effects of boundary-layer thickness will be determined. Finally the details of the three-dimensional flow field will be shown by a combination of various colour figures.

One should be aware that in the experiment the flow is inherently unsteady and highly oscillatory because of the amplification of turbulence fluctuations by the shock system. In the present computation, the Reynolds-averaged Navier–Stokes equations are solved and a symmetry condition is enforced. Therefore the flow is steady and the comparison of computational results with experimental measurements is made only in terms of average values. One expects the surface mean static pressure to be least sensitive to the turbulence fluctuations. The discussion of flow-field features, such as particle paths, should be read with caution.

3.1. *Surface properties and results at the plane of symmetry*

Figure 5(*a*) and (*b*) shows the comparison of surface pressure along the fin leading edge ($\phi = 0°$), and along various ϕ = constant and x = constant lines on the fin. (ϕ is the angle on the fin measured from the nose.) The pressure is referenced to the total pressure behind the normal shock, p_{t2}, at $\phi = 0°$ and $\phi = 45°$, and otherwise is referenced to the free-stream static pressure p_∞. Here $p_{t2} = 11.86\,p_\infty = 0.3428\,p_{t\infty}$. The agreement is very good except that the level of peak pressure is slightly underpredicted. The location of peak pressure is closely predicted. In these two figures, one observes:

(1) The existence of a peak pressure in the nose region.

(2) The appearance of extreme low pressure around $z/D = 0.2$.

(3) An increase of pressure in the direction toward the plate from the position of the minimum.

(4) The extreme low pressure on the fin dies out downstream of the shoulder.

Such features are commonly explained by a simple sketch of the 'inviscid' flow structure in the plane of symmetry (figure 6). The separation shock intersects with the bow shock, resulting in a supersonic jet (which separates two subsonic regions) impinging on the fin surface, and leads to a peak pressure on the fin. This shock–shock intersection is commonly called an Edney type IV interference between the fin bow shock and the separation shock. The pressure decreases below the value of the total pressure behind the normal shock p_{t2}. This feature is attributed to the gradual decrease of stagnation pressure (from free-stream stagnation pressure $p_{t\infty}$ to p_∞ at the wall) in the incoming boundary-layer profile. As the flow expands around the shoulder of the blunt fin, the pressure may even be lower than the free-stream static pressure. Indeed, the minimum of low pressure can be less than $p/p_\infty \simeq 0.4$ near $\phi = 90°$. However, this simplified inviscid-flow argument neglects the important role of the horseshoe vortex, and cannot explain the last two features. Actually, the existence of a pressure peak in the nose region does not have to be caused by the impingement of a supersonic jet. Further details will be discussed later in this paper after more information is presented.

Comparisons of pressure on the flat plate along the line of symmetry and y = constant are shown in figure 7 (*a*)–(*c*). Again, the agreement is very good. All the main features, such as upstream influence, pressure rise due to the separation shock (figure 7 (*a*)) and double pressure peak (figure 7*b* and *c*), are well simulated. (In the experiment, there exists a third small peak for $y/D = 1.0$ and 2.0 which the numerical results fail to show for lack of resolution.) Important questions here are why there is a low-pressure region between the pressure rise due to the separation shock and

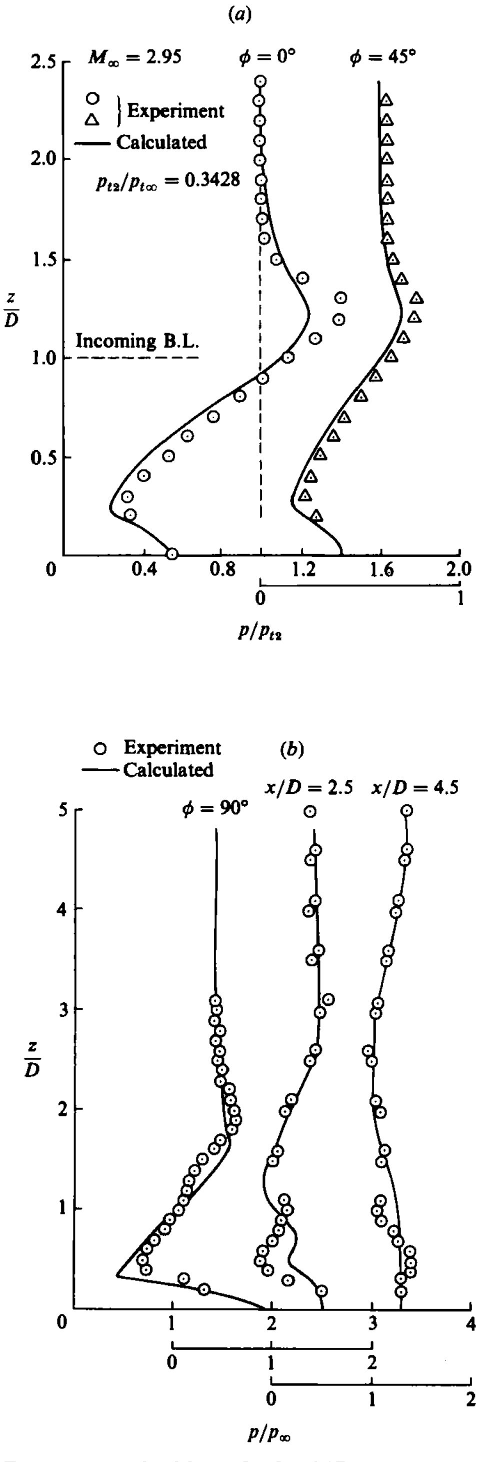

FIGURE 5. Pressure on the blunt fin for $\delta/D = 1.0$: (*a*) along $\phi = 0$ and $\phi = 45$; (*b*) along $\phi = 90$, and $x/D = 2.5$ and 4.5.

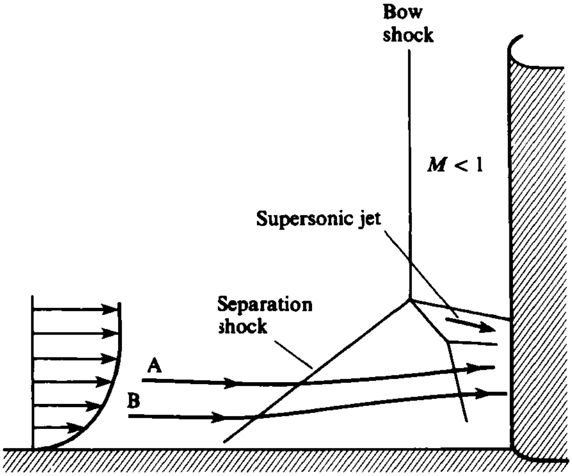

FIGURE 6. A simple sketch of flow structure on the plane of symmetry.

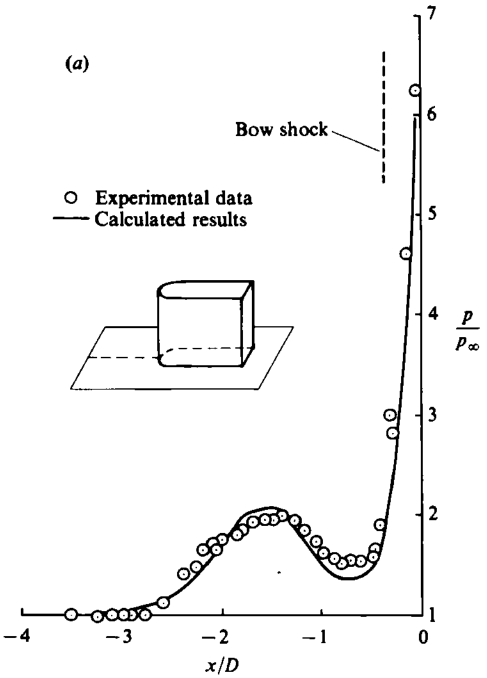

FIGURE 7(a). For caption see facing page.

the final compression along the line of symmetry, and why a double peak appears on the flat plate.

The particle paths in the plane of symmetry (figure 8) clearly show that the flow separates ahead of the blunt fin and spirals to form a primary horseshoe vortex on the plate around the fin. A small secondary vortex near the fin and plate juncture can also be seen. The primary vortex elongates to a length of about 1.5 diameters of the blunt fin with its core only about 0.2 diameters above the flat plate. The

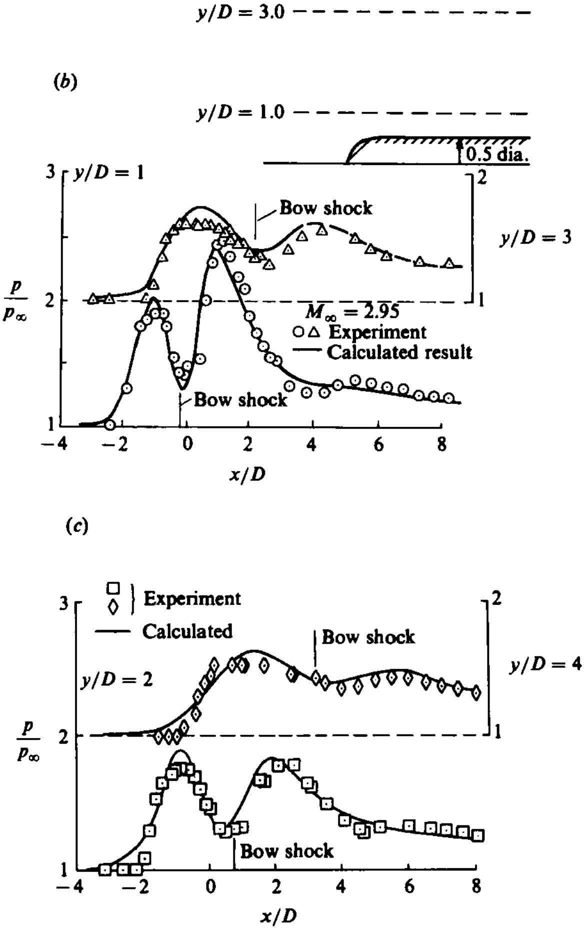

FIGURE 7. Pressure on the flat plate along y = constant ($\delta/D = 1.0$): (*a*) along line of symmetry ($y = 0$); (*b*) along $y/D = 1.0$ and 3.0; (*c*) along $y/D = 2.0$ and 4.0.

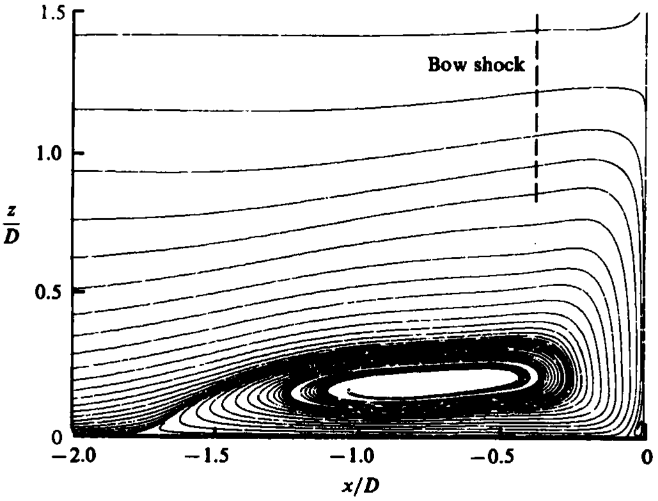

FIGURE 8. Particle paths on the plane of symmetry.

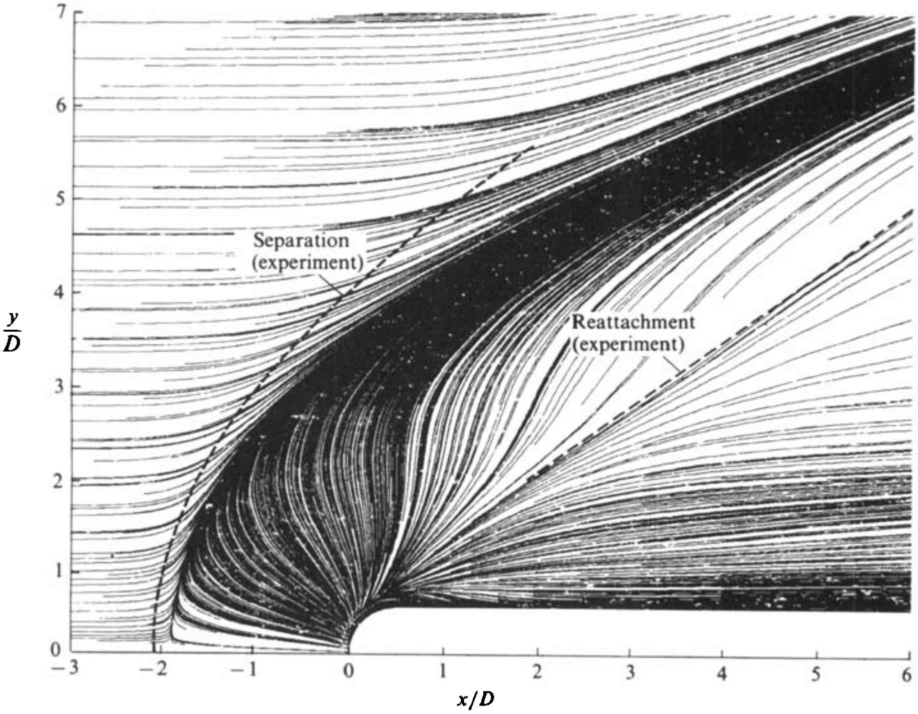

FIGURE 9. Limiting streamlines on the flat plate.

existence of a horseshoe vortex has been clearly shown by Norman (1972) for a low-speed laminar boundary layer over an obstacle. However, although, in supersonic turbulent flow, the existence of a horseshoe vortex has been conjectured from the trace of oil flows it has never been experimentally demonstrated. Figure 9 shows simulated oil-flow lines on the flat plate. The experimental separation and reattachment lines are also marked in the figure. The reattachment line is difficult to define both in the computations and experiment. Therefore the quality of agreement is difficult to judge. The oil-accumulation line in the experiment is treated as a line of separation. Either it is slightly underpredicted in the computation, or the oil-accumulation line in a highly oscillatory flow does not coincide with the 'steady' separation line.

Figure 10(*a*) and (*b*) shows the contour plots of pressure ($p/\gamma p_\infty$) and Mach number in the plane of symmetry. The superimposed particle paths help one to explain the questions raised in figures 5 and 7. Note that, for the case calculated, the separation shock is very weak and smeared; there is no sharp 'triple point' of the intersection of the bow shock with the separation shock. We have observed no strong Mach-number variation behind the bow shock around the peak-pressure region. We have definitely not observed the so-called supersonic jet behind the bow shock, which separates two subsonic regions and impinges on the fin. The location of peak pressure on the fin leading edge coincides with the stagnation streamline. At this Mach number and Reynolds number, the peak pressure observed in figure 5(*a*) might instead be due purely to multi-compression of the smeared separation shock. Unfortunately, the present numerical scheme with the mesh resolution employed is not capable of adequately resolving the structure of a shock–shock intersection; hence this question warrants further investigation.

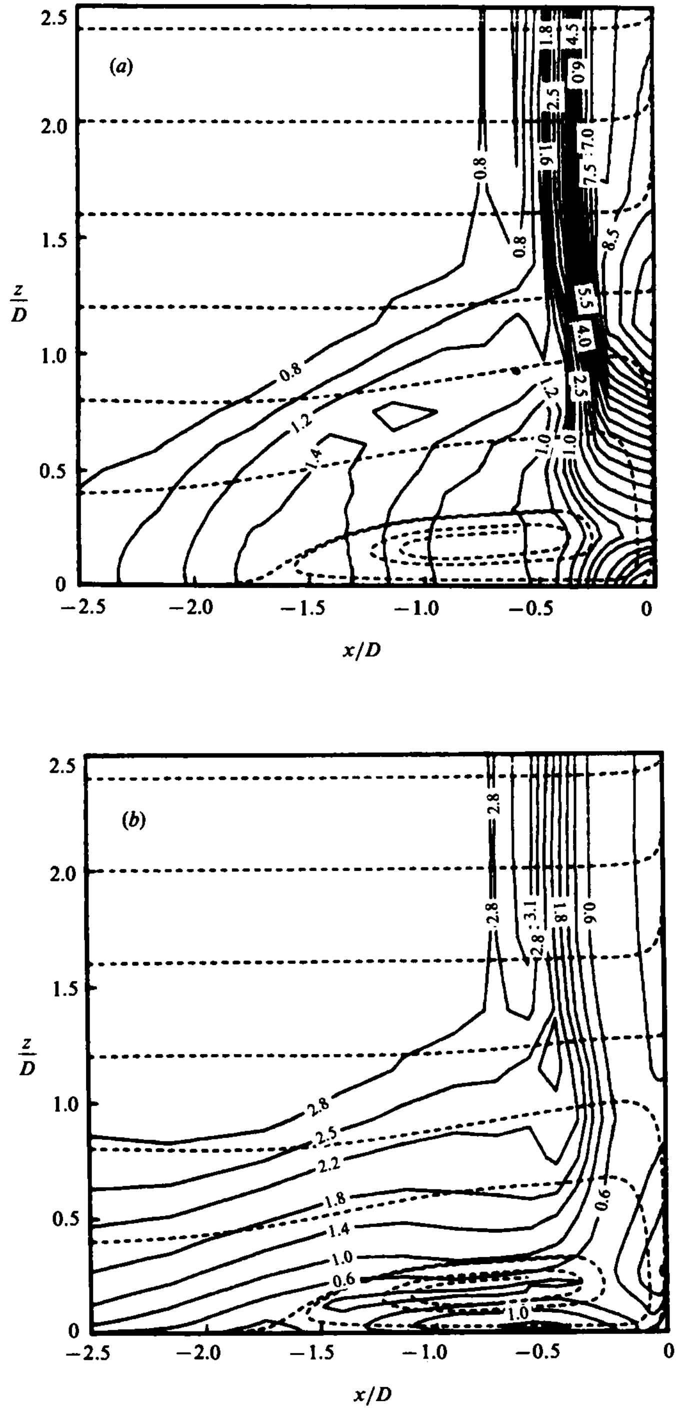

FIGURE 10. Pressure and Mach-number contours on plane of symmetry: (*a*) pressure contours ($p/\gamma p_\infty$); (*b*) Mach-number contours.

The horseshoe vortex brings an abundance of fresh high-momentum fluid into the separation region. (The differences between a three-dimensional spiral-vortex separated flow and a two-dimensional concentric separation pattern were pointed out by Hung & Kordulla (1984).) As this high-momentum fluid accelerates, it results in two reversed-flow supersonic zones; one on the fin, with Mach number as high as 1.2, and another on the plate, with Mach number up to 1.4. The decrease of pressure from the peak to the minimum (figure 5*a*) now is clearly not only a result of the low stagnation pressure in the incoming boundary layer, but also of extreme expansion caused by the horseshoe vortex and leading to a reversed-flow supersonic zone on the fin. Indeed, the streamline of low-momentum flow never directly stagnates on the fin; it is spiralled into the horseshoe vortex (see figure 8). The increase of pressure towards the plate from the minimum is due to recompression from supersonic flow back to subsonic flow. It is this adverse pressure gradient that leads to the generation of a secondary vortex on the fin. As the horseshoe vortex moves laterally away from the fin, the effect of the speed-up from the vortex decreases drastically. That is why the existence of a minimum in pressure disappears as x/D exceeds 1.5 (figure 5*b*). Details of the pressure expansion around the fin, and the existence of separation on the fin are shown in the pressure contour plot and the limiting streamlines on the unwrapped fin surface (figures 11*a* and *b*).

Comparing figures 10(*a*) and (*b*), we see that the two low-pressure regions on the fin and on the flat plate correspond to the two reversed supersonic zones, respectively. This implies that the low pressure immediately aft of the separation shock also is connected to the existence of the reversed high-speed flow region as discussed above. Once we understand the role of the horseshoe vortex in the appearance of a low-pressure region, the appearance of a double peak in pressure on the plate away from the symmetry plane can be explained. Off the line of symmetry the second peak of surface pressure is a result of the expansion as the flow passes over the blunt fin. (An appearance of peak pressure often is caused by a compression followed by an expansion.) The low pressure between two peaks of pressure is caused also by the high velocity near the plate under the core of the vortex. This high velocity and low pressure under the core of a vortex is a phenomenon typical of an image or so-called ground effect of the vortex. It also has often been observed, but seldom explained, in separated crossflows (for instance, figures 6, 10, and 21 of Degani & Schiff 1983). Recently a similar feature of low pressure behind the separation pressure rise has also been observed experimentally in flow over a skewed compression ramp (see figure 4*b* in Teng & Settles 1982).

The existence of two reversed-flow supersonic zones was first observed by Voltenko, Zubkov & Panov (1967). However, they argued that there were two corresponding shocks, one on the fin and one on the plate, to recompress the flow back to subsonic. Based on figure 10(*b*), one might say that there is a shock on the fin due to the appearance of a large variation of Mach number in a short distance; but there is no second shock on the plate (there is enough resolution in that region). The pressure rise to the level of the first peak is due to gradual recompression as shown in the Mach contour plot. The existence of a reversed supersonic region has also been observed in the crossflow about a cone at large angle of attack (e.g. Nebbleling & Bannink 1978).

3.2. *Effect of varying boundary-layer thickness*

In this section the effect of varying boundary-layer thickness will be discussed. The unit Reynolds number is held fixed, while the thickness of the incoming boundary layer is reduced from $\delta/D = 1.0$ to 0.26 and then to 0.10. A boundary-layer profile

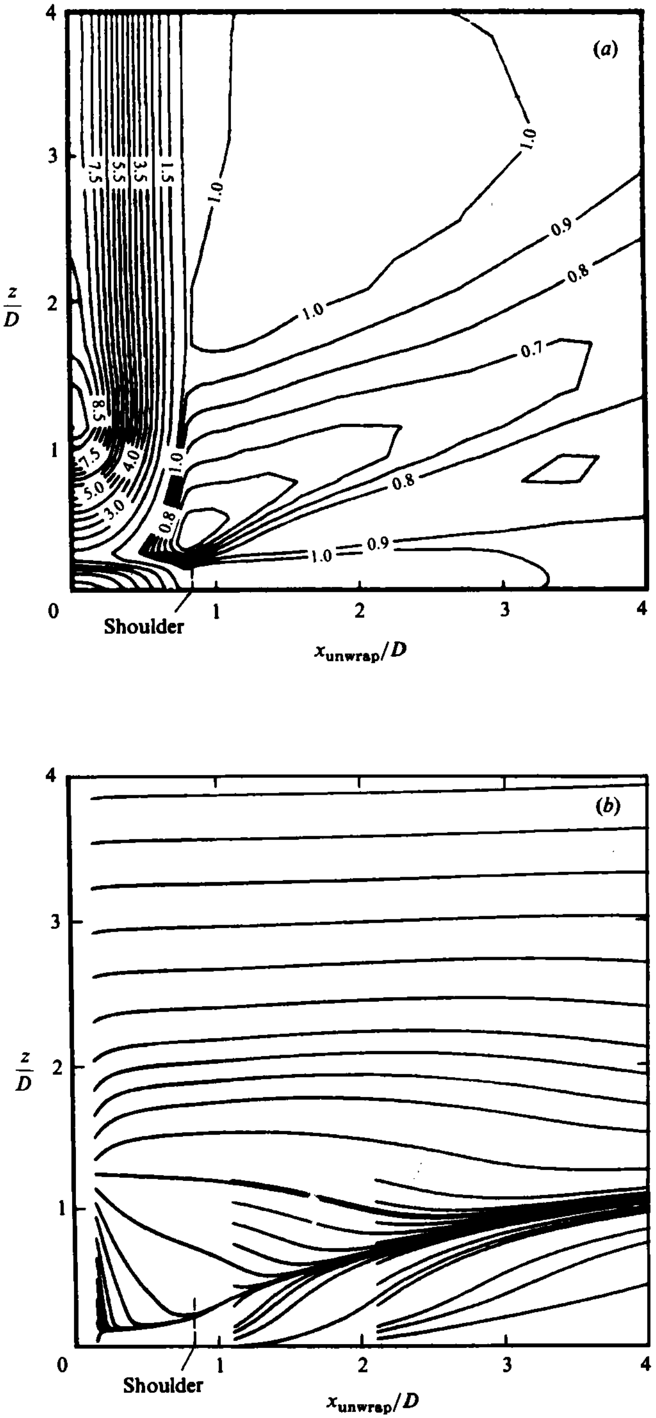

FIGURE 11. Pressure and limiting streamlines on the unwrapped fin surface: (*a*) pressure contours ($p/\gamma p_\infty$); (*b*) limiting streamlines.

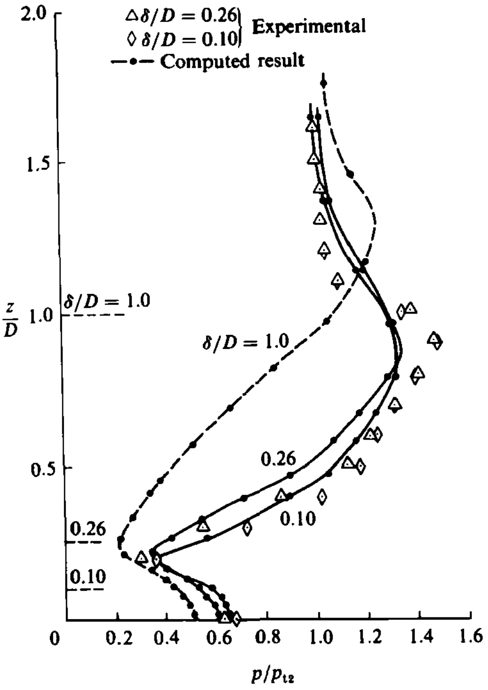

FIGURE 12. Pressure on fin leading edge for different boundary-layer thicknesses: $\delta/D = 0.26$ and 0.10.

and a new mesh with smaller computational domain are generated for the $\delta/D = 0.26$ case. For the case of $\delta/D = 0.10$, the same mesh is used and the boundary-layer profile is assumed similar and is converted from that of the $\delta/D = 0.26$ case, allowing for the smaller boundary-layer thickness. The first mesh point ahead of the interaction is set at about $y+ = 8$ for $\delta/D = 0.26$ and about 12 for $\delta/D = 0.10$. The use of a large value of $y+$ for the thin boundary-layer case is to prevent too much stretching from the fine to the coarse mesh and to provide 'adequate' resolution of the separation line on the plate and of the peak pressure area on the fin.

Figure 12 shows the comparison of computed and measured pressures on the fin leading edge for $\delta/D = 0.26$ and 0.10. The computed results for $\delta/D = 1.0$ are also shown in the figure for comparison. Again the agreement is good. Surface pressures at $\phi = 45°$ and $90°$ (not shown here) are also in similar agreement as shown before. The peak pressure is again under-predicted because of insufficient resolution. (The dot on the line of computed results indicates the mesh resolution.) The main difference between $\delta/D = 1.0$ and 0.26 cases is the change in the location of the peak pressure from about $z/D = 1.25$ to 0.92. The value of peak pressure changes very little, from $p/p_{t2} = 1.22$ to 1.34. Decreasing δ/D further to 0.10 produces only a slight change in the location and level of the peak pressure. An interesting finding is that the location and level of minimum pressure are almost the same for all three cases.

Figure 13(*a–c*) shows comparisons of pressure on the flat plate at $y/D = 0$, 1.0, and 2.0 for $\delta/D = 0.26$. The computed results for $\delta/D = 1.0$ are also plotted in figures 13(*b*) and (*c*) for comparison. The agreement with experiment is again very good. Along the line of symmetry ($y/D = 0$), the computation indicates a decrease of pressure near the corner, as shown in the inset fine-scale plot. Note that, for a

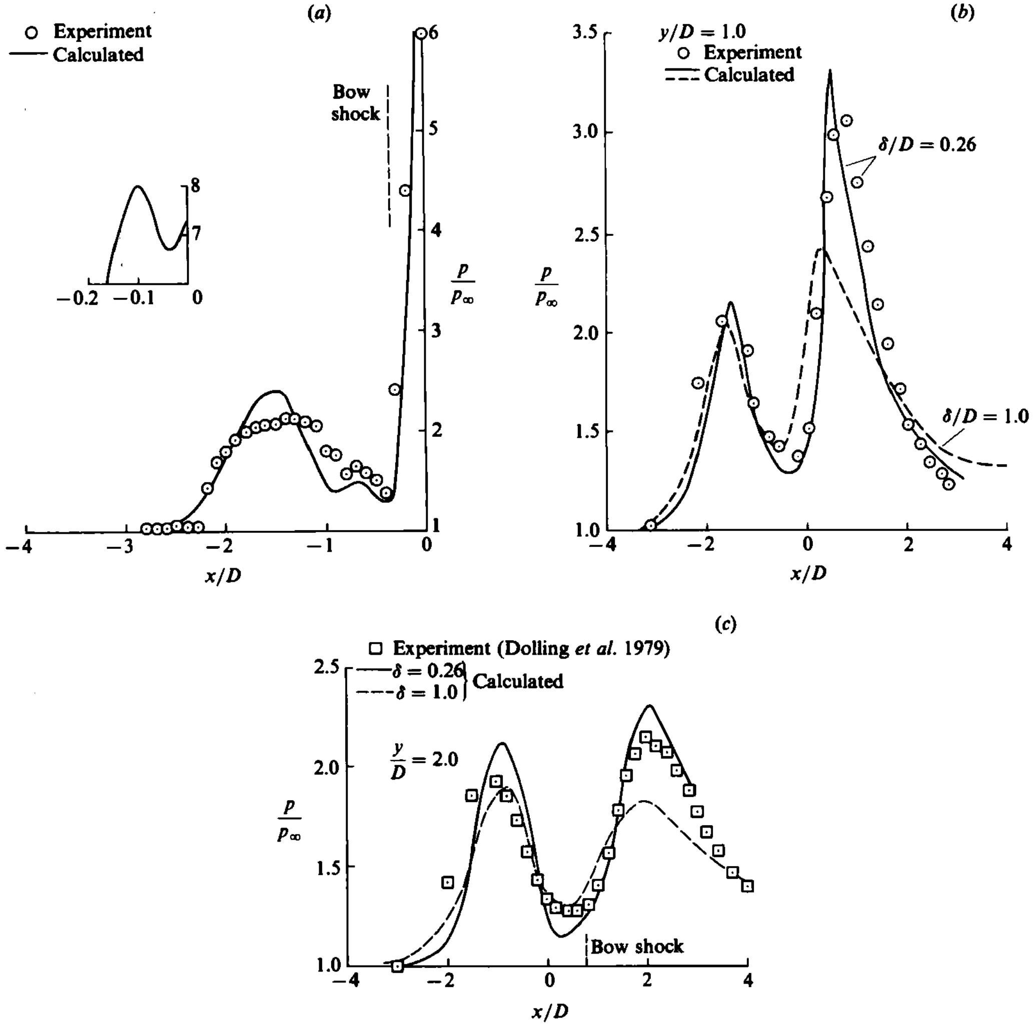

FIGURE 13. Pressure on flat plate for $\delta/D = 0.26$ case: (*a*) along line of symmetry $y = 0$, (*b*) $y = 1.0$; (*c*) $y = 2.0$.

thinner incoming boundary layer, the peak of pressure is higher (figures 13(*b*) and (*c*). The most striking finding is that, while the level of peak pressure is different, the extent of the interaction and the locations of maximum and minimum pressure are very close for the two widely different incoming boundary layers. This feature is confirmed by the experimental observations of Dolling & Bogdonoff (1982).

Figure 14(*a–c*) shows pressure contours, Mach contours, and particle paths for $\delta/D = 0.26$; figure 15 shows Mach contours for $\delta/D = 0.10$. All these figures represent computed results on the plane of symmetry. Comparison of figure 14(*b*) with 10(*b*) shows that, as the incoming boundary layer is made thinner, the lambda shock moves outside the viscous layer and becomes well defined. The location of peak pressure is changed, corresponding to the new location of the intersection of the separation shock with the bow shock. Apart from that, the differences are very minor. The size and location of the horseshoe vortex is about the same (see figures 8 and 14*c*). Even with better definition of separation shock for the thin boundary-layer case,

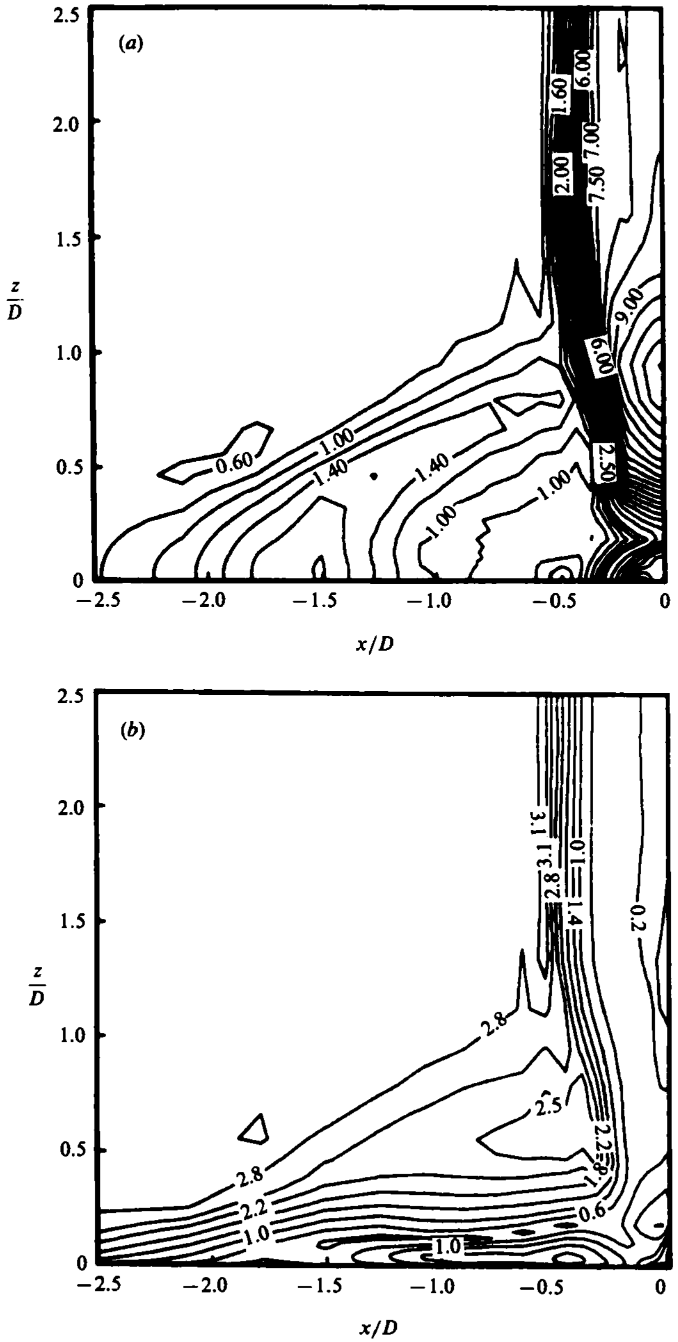

Figure 14(*a*, *b*). For caption see facing page.

we still observe no existence of the so-called supersonic jet. As the boundary-layer thickness decreases further, the Mach number contours show almost no change (compare figures 14*b* and 15). One can conclude that the size and location of the horseshoe vortex are dominated by the inviscid bow shock. Consequently, the location of low pressure on the fin and the extent of the interaction on the plate are all weakly

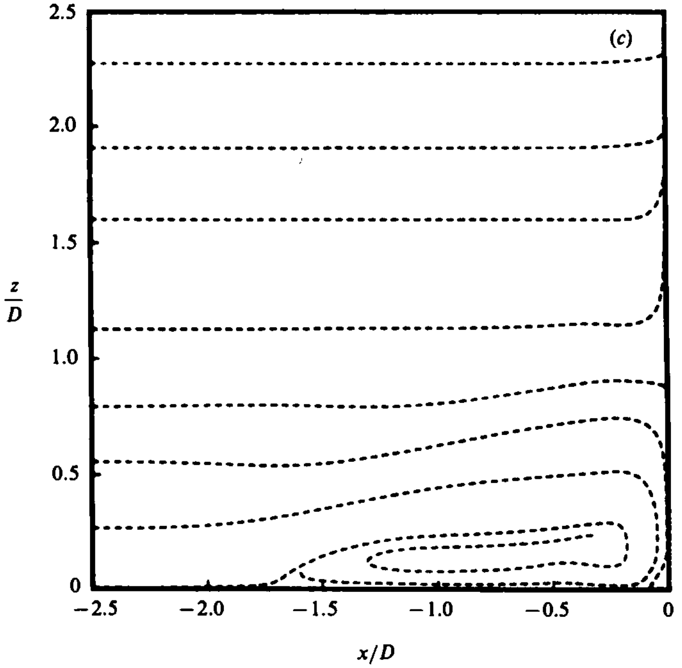

FIGURE 14. Results on plane of symmetry for $\delta/D = 0.26$ case: (*a*) pressure contours; (*b*) Mach-number contours; (*c*) Particle paths.

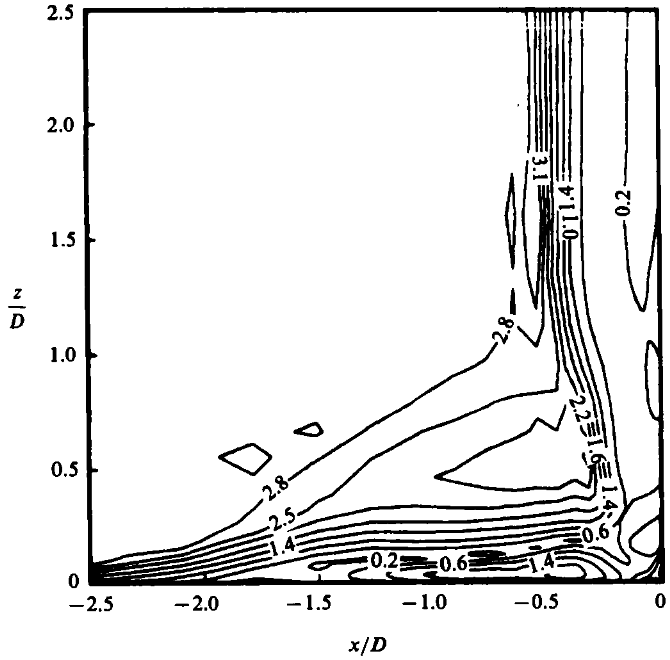

FIGURE 15. Mach-number contours on plane of symmetry for $\delta/D = 0.10$.

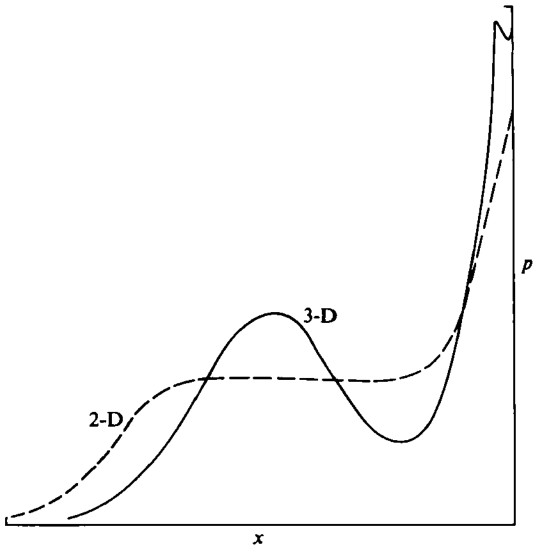

FIGURE 16. Sketch of surface pressure for two-dimensional flow *vs.* three-dimensional blunt fin.

dependent on the thickness of the incoming boundary layer, as observed in figures 13 and 14. The differences in magnitude of pressure on the surface result from the different boundary layers responding to essentially the same size of horseshoe vortex.

To conclude the last two sections, we would like to emphasize a significant difference between the behaviour of surface pressure for two-dimensional flow and three-dimensional flow (figure 16). For a two-dimensional flow (for example, a forward-facing step or a compression ramp) the surface pressure typically reaches a plateau behind the separation pressure rise before the final compression. The range of upstream influence is dependent on the Mach number and Reynolds number, and the level of the plateau pressure is based on the free-interaction theory discussed by Chapman, Kuehn & Larson (1958). If there were a low-pressure region behind the separation pressure rise in two-dimensional flow, one would expect a secondary separation in that region in response to the favourable pressure gradient. In contrast to the two-dimensional case, a three-dimensional flow often exhibits low pressure behind the separation-pressure rise, due to a reversed high-speed flow in the spiral vortex. Near the juncture, there may exist a second peak (as observed in figure 13*a*) because of the existence of a secondary vortex. Away from the plane of symmetry, there is no pressure plateau (see figures 7*b*, *c*, and 13*b*, *c*). Along or near the line of symmetry, there may exist a short region of pressure plateau (see figures 7*a* and 13*a*) but this is not conclusive and needs further investigation. The location of separation for a blunt fin is inviscid dominated and is controlled by the horseshoe vortex. As pointed out by Kaufman *et al.* (1972) (see their figure 20), for a quite wide range of Mach number and Reynolds number, the separation is at about 2.0 diameters ahead of a blunt fin, as long as the incoming boundary layer is turbulent.

3.3. *Details of flow field*

In a three-dimensional flow-field simulation, a tremendous amount of data is generated. Data processing and display have become crucial in our attempts to gain physical insights from these large data bases. In the foregoing discussion, we concentrated on surface quantities and the flow field in the plane of symmetry to gain some understanding of the three-dimensional features, but many questions remain to be answered. In this section coloured graphics are used to show the additional properties of the flow, mainly for the case of $\delta/D = 1.0$.

Figures 17 and 18 (plates 1 and 2) show pressure and Mach-number distributions in a sequence of (J, K)-planes. The magnitudes of pressure and Mach number are indicated in the corresponding colour chart. There are also several contour lines to help show the variation in the magnitude. The pressure and Mach number shown in figures 17(*a*) and 18(*a*) are equivalent to those in figure 10(*a*) and (*b*), except that now the main features such as intensive pressure near the fin leading edge (figure 17*a*) and the two reversed-flow supersonic zones (figure 18*a*) can be easily identified.

Away from the leading-edge symmetry plane and around the shoulder of the fin, the bow shock moves outward and the flow expands. The gradual decrease in pressure and the relative locations of bow shock, separation shock and low-pressure region are clearly shown in figure 17. The response of Mach number to the pressure variation of figure 17 is shown in figure 18. An interesting feature is that, while the Mach number behind the bow shock increases substantially as the flow expands, the Mach number near the plate does not change very much in magnitude and in its variation with height. This indicates that the horseshoe vortex maintains about the same height above the plate, remains confined in the viscous layer, and does not penetrate into the inviscid flow field, as it spirals downstream.

The details of the double peak in pressure are easily observed in the plots of pressure distribution at various z-planes (figure 19, plate 3). Between $z/D = 0.276$ and 0.650, indeed, the pressure exhibits a triple peak due to overexpansion around the shoulder. At around $z/D = 0.950$ the first peak in pressure begins to merge into the second peak. As z/D becomes large, the viscous effects from the flat plate eventually disappear, and the flow resembles a two-dimensional blunt-body solution.

Figure 20 (plate 4) shows the Mach number at various planes of constant z. Very near the plate surface the flow is viscous dominated and subsonic. The low-Mach-number region coincides with the trajectory of the foot trace of the spiral horseshoe vortex, and the high subsonic pocket ($M \geqslant 0.8$) is in the reversed-flow region. Moving away from the surface, most of the flow is supersonic, except for two pockets of subsonic flow, a large one associated with the vortex and a small one in front of the fin. At about $z/D = 0.276$, the two subsonic pockets merge into one and detach from the blunt nose. As z/D becomes large, the subsonic pocket attaches to the blunt nose again. At $z/D = 0.275$ a high-Mach-number region begins to develop on the side of the fin beyond the shoulder. Its peak value may approach the free-stream Mach number because of the expansion around the shoulder. At $z/D = 1.426$, the high-Mach-number region has lifted off the fin, and moved into the middle of the flow field. Below $z/D = 1.426$, the interaction of the boundary layer on the plate with the blunt-fin-induced shock wave is visible. As z/D becomes large, the interaction eventually vanishes, and the flow becomes a typical two-dimensional solution. Taken together figures 17–20 provide a picture of pressure and Mach number in the entire flow field for a blunt-fin-induced shock wave and boundary-layer interaction.

4. Concluding remarks

A supersonic flow over a blunt fin mounted on a flat plate has been simulated numerically. In spite of the limited mesh resolution available and the complicated flow field, the agreement between computed results and measured surface pressure is very good. The role of a horseshoe vortex associated with observed features of the flow has been explored at length. Detailed information on pressure and Mach-number distributions in the flow has been presented.

The study, however, is far from being complete. With respect to the numerical technique, one should keep in mind that the simulated shock was smeared over several mesh points such that it was not possible to resolve a shear layer resulting from a shock–shock impingement. A numerical technique with the capability of capturing shocks more sharply and better mesh resolution are needed. The issue of mesh distribution was not addressed here. Regarding the physical aspects, there are several questions that must be resolved. The problem of intense heat transfer in hypersonic flows is a crucial one for design engineers. What is the flow structure when there are four or more vortices in the field? It remains to be explained why the size of the horseshoe vortex is inviscid dominated and to investigate the effects of the changes of the turbulence model in this flow-field simulation. Since the flow is sensitive to turbulence fluctuation and is inherently unsteady, the most important question is how the flow structure, such as horseshoe vortex and separation line, behaves in a stochastically oscillatory flow field. Further and thorough investigations are required to answer these questions.

REFERENCES

BALDWIN, B. S. & LOMAX, H. 1978 Thin-layer approximation and algebraic model for separated turbulent flows. *AIAA paper* 78–257.

CHAPMAN, D. R., KUEHN, D. M. & LARSON, H. K. 1958 Investigation of separated flows in supersonic and subsonic streams with emphasis on the effect of transition. *NACA Rep.* 1356.

DEGANI, D. & SCHIFF, L. B. 1983 Computation of supersonic viscous flows around pointed bodies at large incidence. *AIAA paper* 83–0034.

DOLLING, D. S. & BOGDONOFF, S. M. 1981 An experimental investigation of the unsteady behavior of blunt fin-induced shock wave turbulent boundary layer interaction. *AIAA paper* 81–1287.

DOLLING, D. S. & BOGDONOFF, S. M. 1982 Blunt fin-induced shock wave/turbulent boundary layer interaction. *AIAA J.* **20**, 1674–1680.

DOLLING, D. S., COSAD, C. D. & BOGDONOFF, S. M. 1979 An examination of blunt fin-induced shock wave turbulent boundary layer interaction. *AIAA paper* 79–0068.

EDNEY, B. 1968 Anomalous heat transfer and pressure distributions on blunt bodies at hypersonic speeds in the presence of an impinging shock. *Aeronautical Research Institute of Sweden, Stockholm, Sweden, Rep.* 115.

HAYAKAWA, K., SMITS, A. J. & BOGDONOFF, S. M. 1984 Hot-wire investigation of an unseparated shock-wave/turbulent boundary-layer interaction. *AIAA J.* **22**, 579–585.

HORSTMAN, C. C., SETTLES, G. S., VAS, I. E., BOGDONOFF, S. M. & HUNG, C. M. 1977 Reynolds number effects of shock-wave turbulent boundary-layer interactions. *AIAA J.* **15**, 1152–1158.

HUNG, C. M. & KORDULLA, W. 1984 A time-split finite-volume algorithm for three-dimensional flowfield simulation. *AIAA J.* **22**, 1564–1572.

HUNG, C. M. & KURASAKI, S. S. 1980 Thin-layer approximation for three-dimensional supersonic corner flows. *AIAA J.* **18**, 1544–1546.

HUNG, C. M. & MACCORMACK, R. W. 1979 Numerical solution of three-dimensional shock wave and boundary layer interaction. *AIAA J.* **16**, 1090–1096.

KAUFMAN, L. G., KORKEGI, R. H. & MORTON, L. C. 1972 Shock impingement caused by boundary layer separation ahead of blunt fin. *ARL* 72–0118, 1972, *Wright-Patterson Air Force Base, Ohio.*

MACCORMACK, R. W. 1982 A numerical method for solving the equations of compressible viscous flow. *AIAA J.* **20**, 1275–1281.

NEBBLELING, C. & BANNINK, W. J. 1978 Experimental investigation of the supersonic flow past a slender cone at high incidence. *J. Fluid Mech.* **87**, 475–496.

NORMAN, R. S. 1972 On obstacle generated secondary flows in laminar boundary layers and transition to turbulence. Ph.D. thesis, Illinois Institute of Technology.

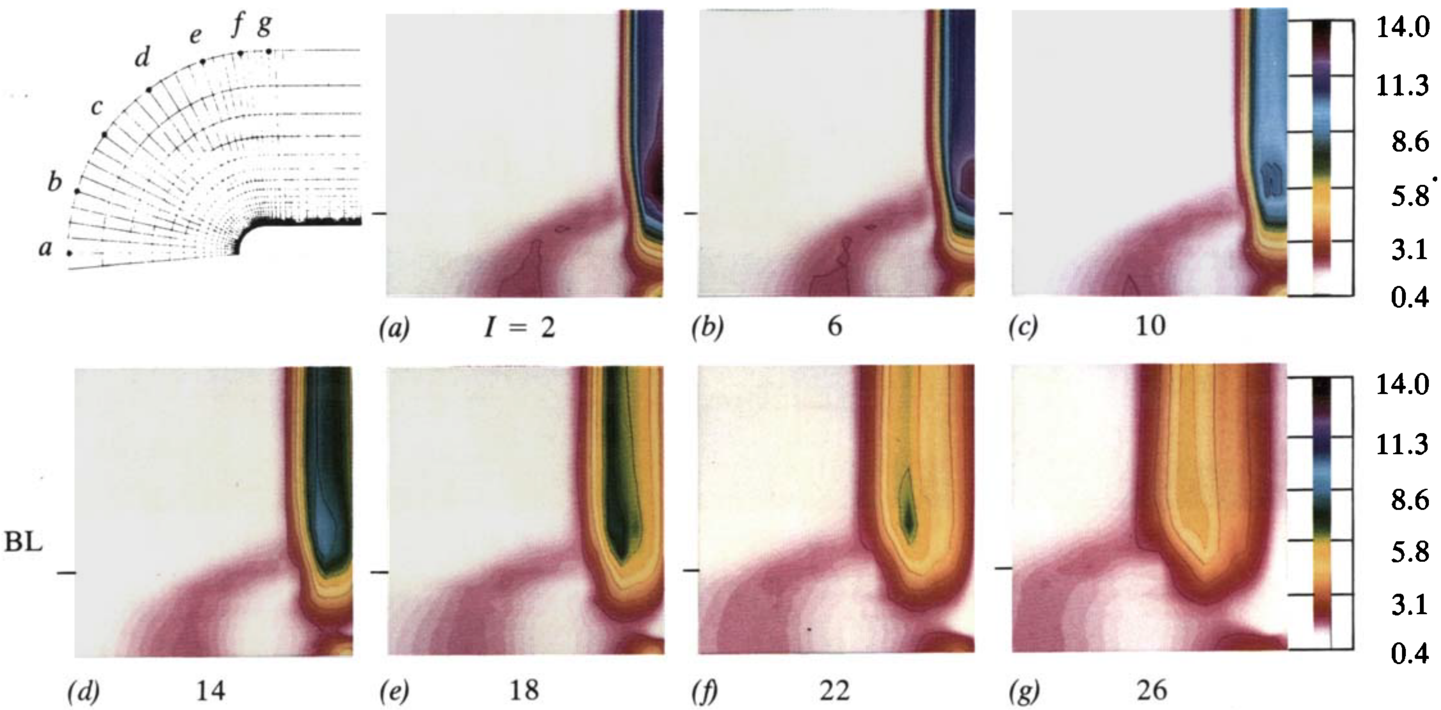

(*a*) $I = 2$ (*b*) 6 (*c*) 10

(*d*) 14 (*e*) 18 (*f*) 22 (*g*) 26

FIGURE 17. Pressure distribution at various (J,K)-planes.

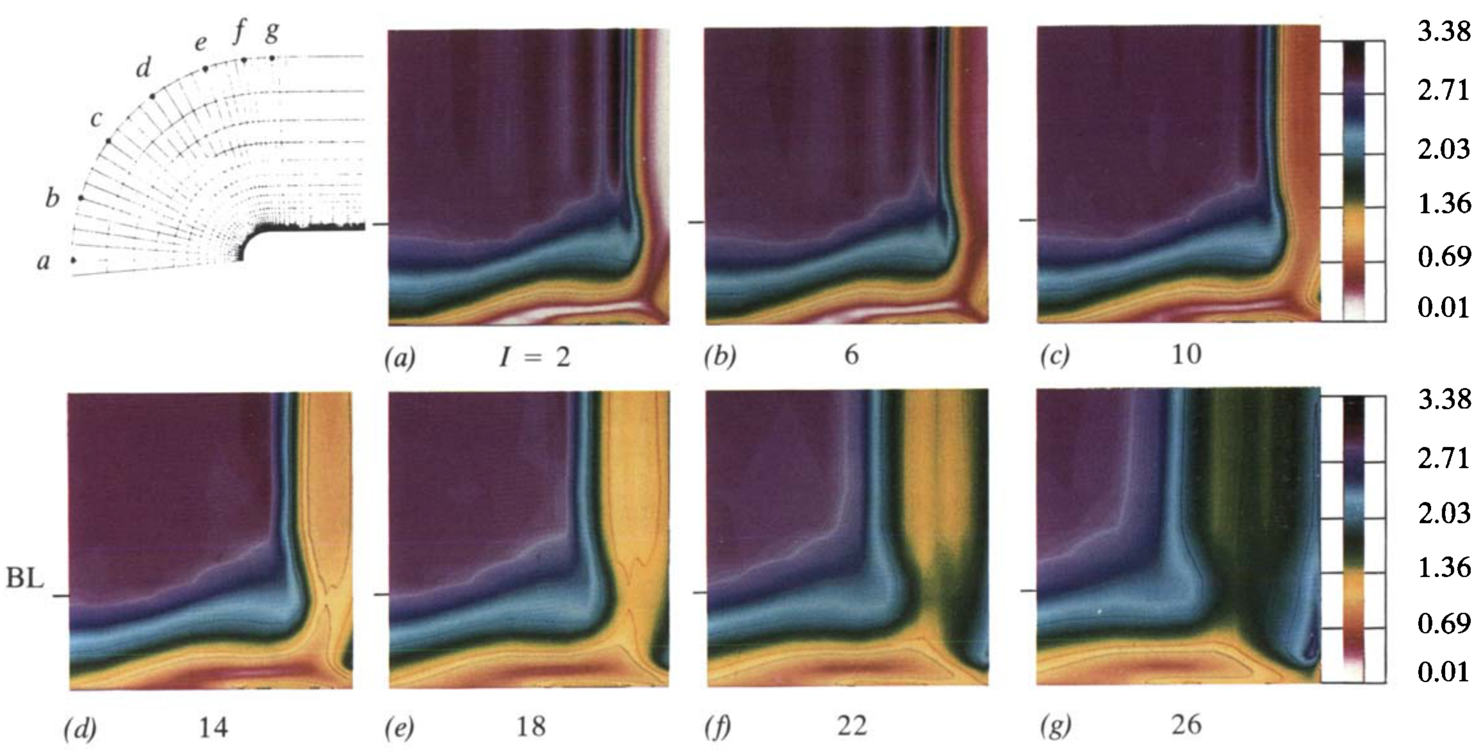

FIGURE 18. Mach number at various (J,K)-planes.

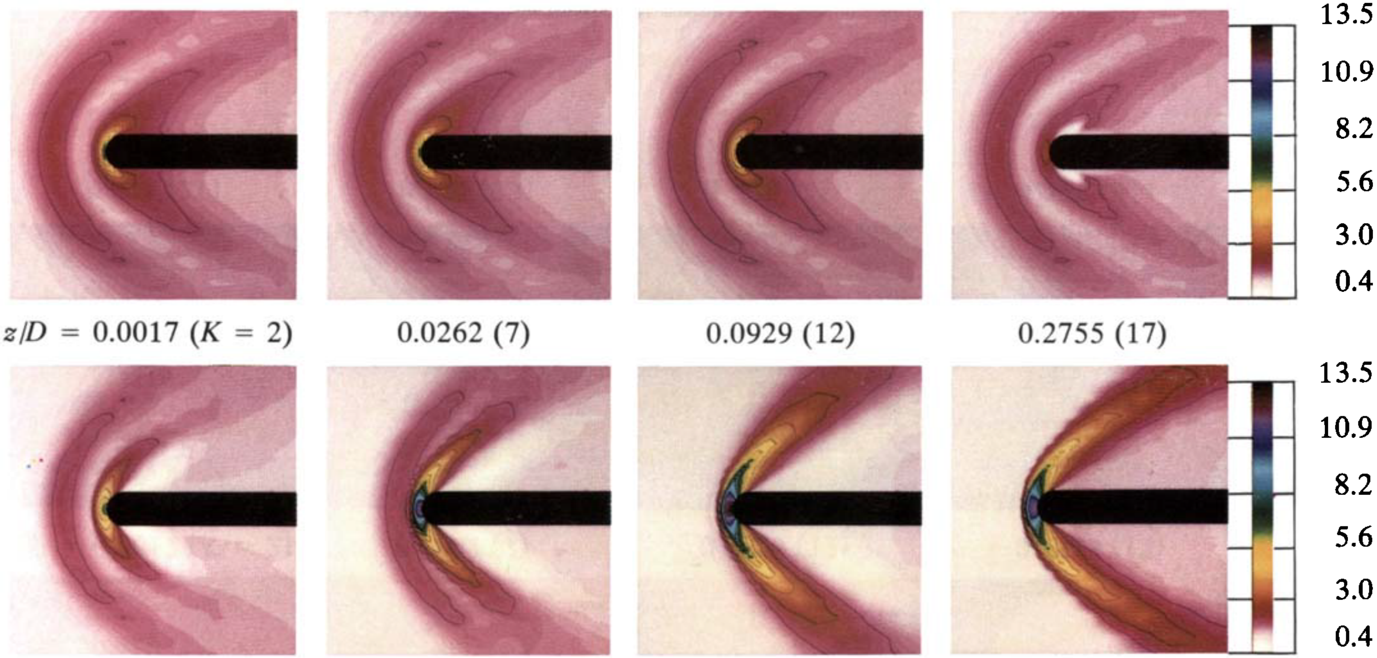

$z/D = 0.0017$ ($K = 2$) 0.0262 (7) 0.0929 (12) 0.2755 (17)

0.631 (21) 0.950 (23) 1.426 (25) 4.770 (31)

FIGURE 19. Pressure distribution at various z = constant planes.

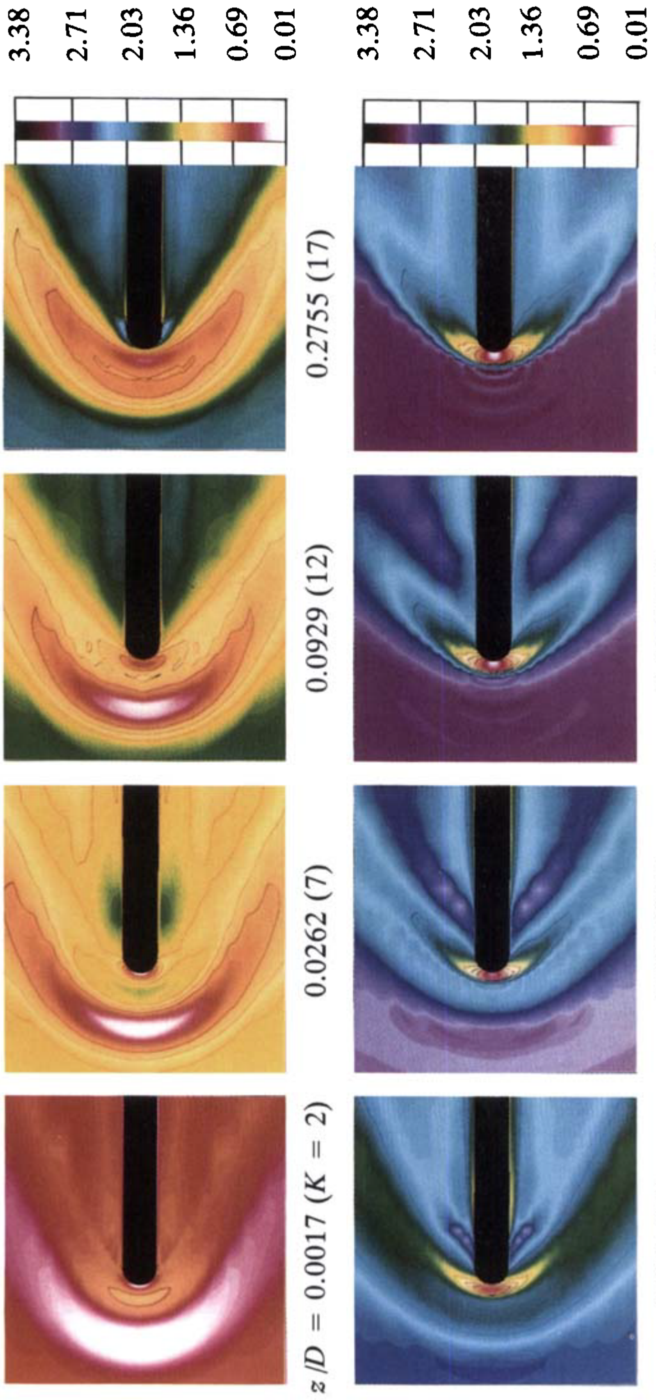

Figure 20. Mach number at various z = constant planes.

OZCAN, K. 1982 An experimental investigation of three-dimensional boundary layer separation in supersonic flow past a circular cylinder on a flat plate. Ph.D. thesis, University of California, Berkeley.

PRICE, A. E. & STALLING, R. L. 1967 Investigation of turbulent separated flows in the vicinity of fin type protuberances at supersonic Mach number. *NASA TN* D-3804.

RUBIN, S. G. 1966 Incompressible flow along a corner. *J. Fluid Mech.* **26**, 99–110.

SEDNEY, R. & KITCHENS, C. W. 1975 The structure of three-dimensional separated flows in obstacle, boundary-layer interactions. *Flow Separation*, AGARD Cp-168, paper 37.

STRANG, G. 1968 On the construction and comparison of difference schemes. *SIAM J. Numer. Anal.* **5**, 506–517.

TENG, H. Y. & SETTLES, G. S. 1982 Cylindrical and conical upstream influence regimes of 3D shock/turbulent layer interactions. *AIAA paper* 82–0987.

VOLTENKO, D. M., ZUBKOV, A. I. & PANOV, YU. A. 1967 The existence of supersonic zones in three-dimensional separated flows. *J. Fluid Dyn.* **2**, 13–16. (Royal Aircraft Establishment Library Translation 1302, 1968.)